

THE LOCATION OF CENTROIDS IN PHOTON AND ELECTRON MAPS OF SOLAR FLARES

MARCO PRATO^{1,2}, A. GORDON EMSLIE³, EDUARD P. KONTAR⁴, ANNA MARIA MASSONE², AND MICHELE PIANA^{2,5}

¹ Dipartimento di Matematica, Università di Modena e Reggio Emilia, via Campi 213/b, I-41100 Modena, Italy; marco.prato@unimore.it

² CNR-INFN LAMIA, via Dodecaneso 33, I-16146 Genova, Italy; massone@ge.infn.it

³ Department of Physics, Oklahoma State University, Stillwater, OK 74078, USA; gordon.emslie@okstate.edu

⁴ Department of Physics & Astronomy, The University, Glasgow G12 8QQ, UK; eduard@astro.gla.ac.uk

⁵ Dipartimento di Informatica, Università di Verona, Cà Vignal 2, Strada le Grazie 15, I-37134 Verona, Italy; michele.piana@univr.it

Received 2009 July 13; accepted 2009 October 14; published 2009 November 6

ABSTRACT

We explore the use of centroid coordinates as a means to identify the “locations” of electron–proton bremsstrahlung hard X-ray sources in solar flares. Differences between the coordinates of the electron and photon centroids are derived and explained. For electron propagation in a collision-dominated target, with either a uniform or an exponential density profile, the position of the electron centroid can be calculated analytically. We compare these analytic forms to data from a flare event on 2002 February 20. We first spectrally invert the native photon visibility data to obtain “electron visibilities,” which are in turn used to construct electron flux images at various electron energies E . Centroids of these maps are then obtained by straightforward numerical integration over the electron maps. This comparison allows us to infer the density structure in the two compact sources visible, and we discuss the (somewhat unexpected) results thus obtained.

Key words: methods: data analysis – Sun: flares – Sun: X-rays, gamma rays – techniques: image processing

1. INTRODUCTION

It is generally accepted that most of the essential physics related to particle acceleration and propagation occurs on size scales that are several orders of magnitude below achievable resolution. Because of the many-order-of-magnitude discrepancy between the size scales on which particle acceleration processes occur and the size scales that can be effectively resolved, most results have concerned themselves with measuring various *moments* of the source spatial structure on observable scales—e.g., “intensity” (zeroth moment), “location” (first normalized moment), “size” (second normalized moment), and “asymmetry” (related to the third normalized moment).

Although various other measures (e.g., the location of peak intensity, the peak of a best-fit Gaussian form) can also be used to define the “location” of a source, we here suggest, in view of its inherent relation to normalized moments, that the most natural measure of the “location” of such a source is the first normalized moment, i.e., the *centroid*. The use of the centroid as an indicator of the location has further advantages:

1. Observation of the location of peak intensity requires, in general, an instrument with high spatial resolution, whereas the centroid, which is related to integral moments, may be readily determined using an instrument with relatively coarse spatial resolution.
2. Characterizing the location of the source through the position of the peak of a best-fit Gaussian implicitly imposes a source symmetry that may not be (and in general is not) present; by contrast, determining the centroid position requires no such assumption of symmetry.

The ability to characterize the spatial structure of solar flare hard X-ray emission as a function of photon energy has proven most effective in constraining models for particle acceleration and transport. Using data from *RHESSI* (Lin et al. 2002), Hurford et al. (2003) have shown that the locations of the principal hard X-ray and gamma-ray sources in the 2002

July 23 event are not cospatial, an observation that points to different sites for electron and proton acceleration (Emslie et al. 2004). Xu et al. (2008) have considered the variation of source *size* and *shape* with photon energy; they thereby deduced the extent and density of, and hence number of particles in, the electron acceleration region.

The studies of Hurford et al. (2003) and Xu et al. (2008) were concerned mostly with analysis of extended sources, for which terms like source *size* and *asymmetry* have meaningful significance. However, many flares exhibit a different geometry, especially at higher energies $\gtrsim 10$ –30 keV, such as a small number of discrete “footpoint” sources. As shown by Brown et al. (2002) and Aschwanden et al. (2002), such simple sources are well characterized by a single energy-dependent coordinate pair that characterizes the location of maximum brightness. Kontar et al. (2008) have used observed subarcsecond variations in the characteristics of hard X-ray sources to infer the source *sizes* (second moments) that determine the magnetic field structure in the chromosphere, a quantity unavailable to traditional observational techniques.

It must be stressed that the locations of the observable *radiation* from flares may not be a good indicator of the locations where the acceleration of the *particles* takes place. For example, electrons accelerated in a relatively tenuous “acceleration region” may have to propagate some distance before encountering a target of sufficient density to produce observable hard X-ray emission; thus the characteristics (density, magnetic field, geometry) of the region where the hard X-ray emission is observed may have little or no relationship to the same parameters in the acceleration region itself. It is therefore important to distinguish between the centroids of the electron distribution and the resulting radiation field, and we explicitly address this point in this paper.

In Section 2, we present simple analytic formulae for the positions of the *centroids* (first moments) of both the photon and electron distributions, and we quantify the above statement regarding the different positions of the flare “locations.” In Section 3, we use the variation of the centroid of the electron

flux image (Piana et al. 2007) to infer the density structure of a compact source in the 2002 February 20 event. In Section 4, we present our conclusions.

2. LOCATIONS OF PHOTON AND ELECTRON FLUX CENTROIDS

We first briefly review the physics of the propagation of energetic electrons in a thick target (Brown 1972; Emslie 1978). Let electrons with an initial flux spectrum $F_0(E_0)$ (electrons $\text{cm}^{-2} \text{s}^{-1} \text{keV}^{-1}$) injected at $s = 0$ and suffer energy loss due to Coulomb collisions with electrons in the ambient medium. The equation of motion for an individual electron is

$$\frac{dE}{ds} = -\frac{Kn(s)}{E}, \quad (1)$$

where $n(s)$ is the density distribution of the surrounding plasma and $K = 2\pi e^4 \Lambda$, where e is the electronic charge (esu) and Λ is the Coulomb logarithm. For an electron of an initial energy E_0 , the solution to Equation (1) is

$$E^2 = E_0^2 - 2KN(s), \quad N(s) = \int_0^s n(s') ds', \quad (2)$$

where $N(s)$ is the *column depth* along the electron path. Using flux conservation $F(E, s) dE = F_0(E_0, 0) dE_0$, one readily finds the electron flux spectrum $F(E, s)$ (electrons $\text{cm}^{-2} \text{s}^{-1} \text{keV}^{-1}$) at a general point s in the target:

$$F(E, s) = \frac{E}{\sqrt{E^2 + 2KN(s)}} F_0(\sqrt{E^2 + 2KN(s)}) \quad (3)$$

(Emslie & Smith 1984). Equation (3) depends on the density structure $n(s)$ and is in general a decreasing function of distance for all E . For the specific case of a power-law form $F_0(E_0) = F_b(E_0/E_b)^{-\delta}$ (where F_b is the flux at (arbitrary) reference energy E_b),

$$F(E, s) = (F_b E_b^\delta) E [E^2 + 2KN(s)]^{-(\delta+1)/2}. \quad (4)$$

Note that the appearance of the E^2 term in the square brackets is purely a consequence of the assumption of collisional energy losses, i.e., of the form of the energy loss rate (Equation (1)); we shall return to this point below.

The observed photon flux spectrum per unit length along the line of sight (photons $\text{cm}^{-2} \text{s}^{-1} \text{keV}^{-1} \text{cm}^{-1}$) is (Aschwanden et al. 2002; Brown et al. 2002)

$$I(\epsilon, s) = \frac{A}{4\pi R^2} \int_\epsilon^\infty n(s) F(E, s) Q(\epsilon, E) dE, \quad (5)$$

where A (cm^2) is the cross-sectional area of the loop in which the electrons propagate, $R = 1 \text{ AU}$, and $Q(\epsilon, E)$ ($\text{cm}^2 \text{keV}^{-1}$) is the solid-angle-averaged⁶ bremsstrahlung cross section, differential in photon energy ϵ , which is finite only for $E \geq \epsilon$. As we shall show below, the contribution of electrons of all energies $E \geq \epsilon$ to the emission at photon energy ϵ leads to a somewhat more extended photon emission at energy ϵ than the corresponding electron source at energy $E = \epsilon$.

⁶ Although the bremsstrahlung cross section is intrinsically anisotropic (Massone et al. 2004), observations (Kontar & Brown 2006) indicate that the target-averaged electron spectrum may well be nearly isotropic, so that the use of an isotropic form of $Q(\epsilon, E)$ gives the correct answer for the observed radiation field.

For a prescribed density structure $n(s)$, Equations (4) and (5) permit a relatively straightforward calculation of the spatial locations of the *maxima* in both $F(E, s)$ and $I(\epsilon, s)$. Alternatively, the observed positions of these maxima may be used to *infer* the density structure: Aschwanden et al. (2002) and Brown et al. (2002) forward-fit parametric two-dimensional Gaussian sources to the observed *RHESSI* modulated light curves of a limb flare at various photon energies ϵ , and used the energy-dependent position of the center of the best-fit Gaussian to determine the density profile of the target atmosphere. In their analysis, they assumed that s , the parameter along the direction of maximum energy loss, corresponded to depth z . Also, although the intensity profile $I(\epsilon, z)$ is intrinsically asymmetric, they used the center of the best-fit Gaussian to the emission profile $I(\epsilon, z)$ as an approximation for the position of maximum intensity. Fitting the data to the form (Equation (5)) allowed them to estimate the form of $n(z)$, i.e., the variation of target density with depth.

As discussed in Section 1, from a *physical* viewpoint, a more natural representation of the “location” of a flare is neither the location of the maximum in $I(\epsilon, s)$ (or in $F(E, s)$), nor the center of the best-fit Gaussian, but rather the (energy-dependent) *centroid* of the brightness distribution function $I(\epsilon, s)$ (or of the electron flux distribution $F(E, s)$).

2.1. Homogeneous Target

For a homogeneous target of density n_0 , it is straightforward to compute the centroid of both $F(E, s)$ and $I(\epsilon, s)$. The centroid of the *electron flux* at a given electron energy E is given by

$$s_c^E = \frac{\int_{s=0}^{s_{\max}} s F(E, s) ds}{\int_{s=0}^{s_{\max}} F(E, s) ds} = \frac{1}{n_0} \frac{\int_{N=0}^{N_{\max}} N F(E, N) dN}{\int_{N=0}^{N_{\max}} F(E, N) dN}, \quad (6)$$

where s_{\max} and N_{\max} are respectively the length and column density of the target. With $F(E, N)$ given by Equation (4), we obtain from Equation (6)

$$s_c^E = \frac{E^2}{Kn_0} \frac{1}{(\delta-3)} \frac{1 - (1+x)^{(1-\delta)/2} (1 + \frac{\delta-1}{2} x)}{1 - (1+x)^{(1-\delta)/2}}, \quad (7)$$

where $x = 2KN_{\max}/E^2$. (Expression (7) is clearly valid only if $\delta > 3$; for values of $\delta \leq 3$ it diverges.⁷) As $N_{\max} \rightarrow \infty$,

$$s_c^E \rightarrow \frac{E^2}{Kn_0(\delta-3)}. \quad (8)$$

Using Equations (4) and (5), with a Kramers approximation $Q(\epsilon, E) = Q_0/\epsilon E$ and $N_{\max} = \infty$, the one-sided centroid of the *photon* emission is located at a column density

$$\begin{aligned} s_c^\epsilon &= \frac{\int_0^\infty s ds \int_\epsilon^\infty (E^2 + 2Kn_0s)^{-(\delta+1)/2}}{\int_0^\infty ds \int_\epsilon^\infty (E^2 + 2Kn_0s)^{-(\delta+1)/2}} \\ &= \frac{\epsilon^2}{Kn_0} \frac{(\delta-2)}{(\delta-3)(\delta-4)} \end{aligned} \quad (9)$$

⁷ This divergence, even in the presence of a finite total electron energy content (for $\delta > 2$), results from the form of the numerator of Equation (6), coupled with the E^{-2} dependence of the Coulomb energy loss cross section; for a more general energy loss process, with a cross section behaving like $E^{-\beta}$, it is straightforward to show that the centroid diverges for $\delta \leq \beta + 1$. A similar situation results in expression (9) for the centroid of the hard X-ray emission (Xu et al. 2008), which is finite only for $\delta > 4$.

(cf. Equation (12) of Xu et al. 2008). From Equations (7) and (9), we see that, for a uniform target of (effectively) infinite extent,

$$\frac{s_c^\epsilon}{s_c^E} = \frac{(\delta - 2)}{(\delta - 4)} \left(\frac{\epsilon}{E} \right)^2, \quad (10)$$

i.e., that the centroid of the photon emission for a given energy ϵ occurs at a greater distance from the acceleration site than the centroid in the electron flux distribution at electron energy $E = \epsilon$. Physically, this is because the emission at photon energy ϵ is a weighted sum of the electron flux at energies $E \geq \epsilon$.

2.2. Exponential Atmosphere

A reasonable parametrization of the density structure for chromospheric footprint sources is the exponential atmosphere form

$$n = n_0 e^{s/H}, \quad (11)$$

where H is the scale height and n_0 is the density at $s = 0$, the upper boundary of the target. The corresponding form of the column density variation is

$$N = N_0 + n_0 H [e^{s/H} - 1], \quad (12)$$

where N_0 is the column density overlying the top of the target (i.e., over $s < 0$). Solving Equation (12) for $s(N)$ and substituting into the centroid Equation (6), with the form (3) for the electron flux, gives

$$s_c^E = \frac{\int_0^\infty s (E^2 + 2KN[s])^{-(\delta+1)/2} ds}{\int_0^\infty (E^2 + 2KN[s])^{-(\delta+1)/2} ds}. \quad (13)$$

This reduces to

$$s_c^E = \frac{(\delta - 1)}{2} H x_0^{\frac{\delta-1}{2}} \int_{x_0}^\infty \ln \left[1 + \frac{(x - x_0)}{2Kn_0H} \right] x^{-(\delta+1)/2} dx, \quad (14)$$

where⁸ $x_0 = E^2 + 2KN_0$. Equation (14) provides s_c^E as a function of the electron energy E and the parameter set (δ, H, n_0, N_0) . The value of δ may be straightforwardly deduced from measuring the spectral index γ of the spatially integrated hard X-ray spectrum and using the thick-target result (Brown 1971) $\delta = \gamma + 1$. We treat the other three parameters as unknowns, to be determined through comparison of expression (13) with observations.

Figure 1 shows the values of s_c^E (in arcseconds), as a function of E^2 , deduced from Equation (14) with $\delta = 3$. For a fixed (H, n_0) , as the amount of overlying material increases, the variation of the centroid position with energy becomes less pronounced, a consequence of the fact that over the range of electron energies in the source, the range of injected electron energy is reduced. For example, for electrons of energy 10–100 keV, the range in injected energies is (trivially) 10–100 keV (a range of 90 keV) for $N_0 = 0$, while for $N_0 = 10^{21} \text{ cm}^{-2}$ ($2KN \simeq 5200 \text{ keV}^2$), the formula Coulomb energy loss formula (2) yields a range of E_0 from ~ 73 to 123 keV (a range of only 50 keV). As the scale height H increases, the rate of density increase is reduced and the differential penetration of higher energy electrons becomes more pronounced. Although Equation (14) shows that this variation of s_c^E is not *strictly* linear

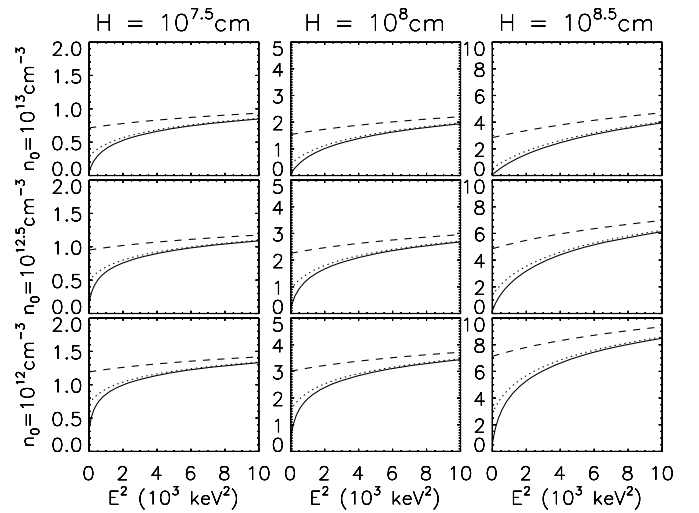


Figure 1. Variation of centroid location s_c^E (arcseconds) with electron energy E for a target with exponential density variation $n = n_0 e^{s/H}$, for various values of the target scale height H , upper boundary density n_0 , and overlying column density N_0 . A spectral index $\delta = 3$ was used. The different figures are for the values of H and n_0 indicated in the upper and left margins; the various lines (solid, dotted, dashed) in each figure correspond to $N_0 = 10^{19}, 10^{20}$, and 10^{21} cm^{-2} , respectively.

with H (H also appears in the quantity x_0), Figure 1 shows that a linear scaling is, for the parameter range involved, a reasonable approximation. Finally, as the target density n_0 increases, the range of all electrons, and so the value of the centroid position, becomes smaller. For high upper boundary densities $n_0 \gg E^2/2KH$, the logarithmic quantity in Equation (14) can be approximated by $\ln(1+x) \sim x$ and the variation of s_c^E with x becomes inversely proportional to n_0 , as expected from Equation (1).

3. APPLICATION TO DATA

We have analyzed the variation of the centroid position with energy for the 2002 February 20 flare (11:06:00–11:06:40 UT). This is one of the first solar flare events observed by *RHESSI*, and the variation of the footprint position with energy for this event has already been studied by Aschwanden et al. (2002) and Brown et al. (2002), using a forward-fit method. The flare occurred near the West limb and has a typical impulsive profile with thermal and nonthermal components of X-ray spectra detectable up to ~ 100 keV. The general structure (see Figure 2 of Aschwanden et al. 2002) shows two footpoints of roughly equal brightness, which we shall label “north” and “south,” indicating their general positions in the image. The spectral index γ for the spatially integrated emission for this event was $\gamma \simeq 3.2$, corresponding (Brown 1971) to an injected electron flux with spectral index $\delta = \gamma + 1 = 4.2$.

As discussed by Hurford et al. (2002), the “natural” form of the *RHESSI* data is a series of “visibilities” (i.e., two-dimensional spatial Fourier components). The (discrete) spatial frequencies $\mathbf{k} = (u, v)$ at which visibility information is obtained form a set of nine concentric circles (one for each of *RHESSI*’s Rotating Modulation Collimators (RMCs)) in the (u, v) -plane. It has been shown (Kontar et al. 2008) that the direct use of photon visibilities, rather than the images that can be reconstructed from them, can boost the angular resolution attainable to as fine as ~ 0.2 , thus allowing a detailed study of the vertical structure of footprint sources located near the

⁸ For completeness, a calculation of the position of the maximum in the density-weighted electron flux, for the density profile (Equation (11)) is provided in the Appendix.

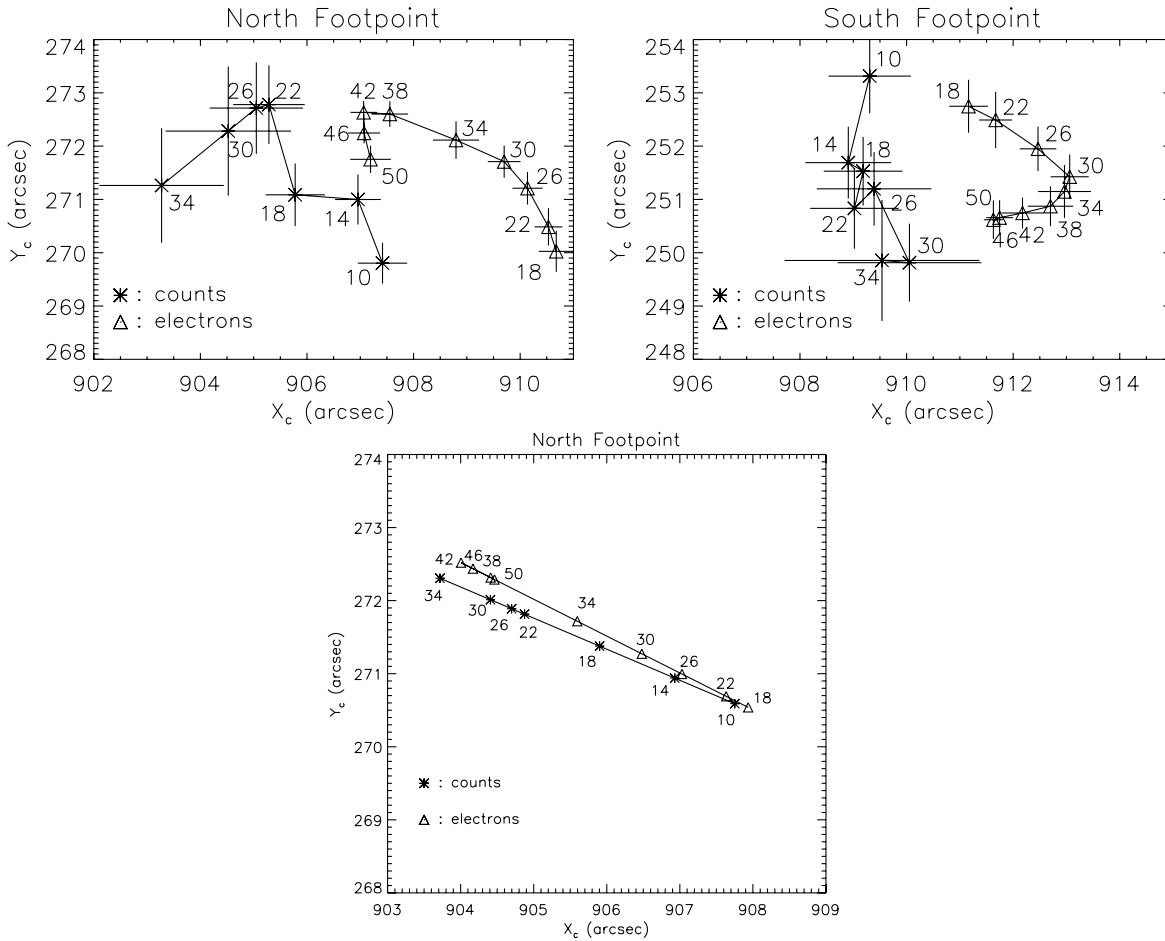


Figure 2. Top panels: positions (with 1σ uncertainties) of the source centroids, in both count and electron domains, for the “north” footpoint (left) and “south” footpoint (right), labeled with the count and electron energies appropriate. (For clarity of presentation, the positions of the electron centroids have been displaced $3''$ to the right in each panel.) Bottom panel: projected positions of the centroids of the “north” footpoint onto the mean trend line, in both count and electron domains, labeled with the count and electron energies appropriate.

solar limb (for which vertical motion on the Sun corresponds to radial displacement in the plane of the sky). Further, as shown by Piana et al. (2007), the inherent linearity in the Fourier transform allows a regularized spectroscopic inversion process to be applied to visibilities in the *count* domain in order to yield the corresponding visibilities in the *electron* domain. These visibilities correspond to the quantity $N(x, y) \bar{F}(x, y; E)$, where $\bar{F}(x, y; E)$ (electrons $\text{cm}^{-2} \text{s}^{-1} \text{keV}^{-1}$) is the mean electron flux spectrum along the line of sight at the point (x, y) in the imaging plane and $N(x, y)$ (cm^{-2}) is the line-of-sight-integrated column density at that location. “Electron flux” images of the quantity $N(x, y) \bar{F}(x, y; E)$ may be obtained from electron visibility data in a manner identical to that used to construct count maps from count visibilities.

We used the visibility-based `uv_smooth` algorithm (Massone et al. 2009) to produce photon (electron) images from the corresponding photon (electron) visibilities in the 2002 February 20 event, and then calculated the centroids by direct integration over the subregions of interest. The results are shown in the top panels of Figure 2.

Consistent with the findings of Aschwanden et al. (2002), we find that both footpoint sources show considerable variation of the centroid position with energy. For the “south” footpoint, the images reveal it to be divided into two subregions, the relative intensity of which is energy dependent. This leads to a rather complicated variation of the centroid position with

energy (the right panel of Figure 2), although there is still a general systematic change of the centroid position with energy. For the “north” footpoint (the left panel of Figure 2), the position of the centroid varies more monotonically with energy (either count or electron). In the bottom panel of Figure 2 we show the positions of both count and electron centroids for the “north” footpoint as a function of energy, projected onto the mean trend line. The behaviors are consistent with Equation (10), in that the centroid position s_c^ϵ at a given count energy ϵ is in general located at a greater depth than the centroid s_c^E of the electron distribution at energy $E = \epsilon$. As discussed in Section 2, this is a result of the emission at photon energy ϵ resulting from electrons at all energies $E \geq \epsilon$.

In Figure 3 we present a comparison of the projected electron centroid positions s_c^E with the analytic result (Equation (14)). The best-fit values for the upper boundary density n_0 , the overlying column density N_0 , and the density scale height H are $[n_0, N_0, H] = [2.2 \times 10^{11} \text{ cm}^{-3}, 2.5 \times 10^{17} \text{ cm}^{-2}, 5.0 \times 10^8 \text{ cm}]$, and $[1.6 \times 10^{11} \text{ cm}^{-3}, 6.3 \times 10^{19} \text{ cm}^{-2}, 3.5 \times 10^8 \text{ cm}]$, for the “north” and “south” footpoints, respectively. We note the following.

1. The values for $n_0 \sim (1.9 \pm 0.3) \times 10^{11} \text{ cm}^{-3}$ are not only comparable, but correspond well to the values in both empirical (see Figure 10 of Aschwanden et al. 2002 and Table 3 of Machado et al. 1980) and theoretical (see Figure 1 of Mariska et al. 1989) solar flare atmosphere models.

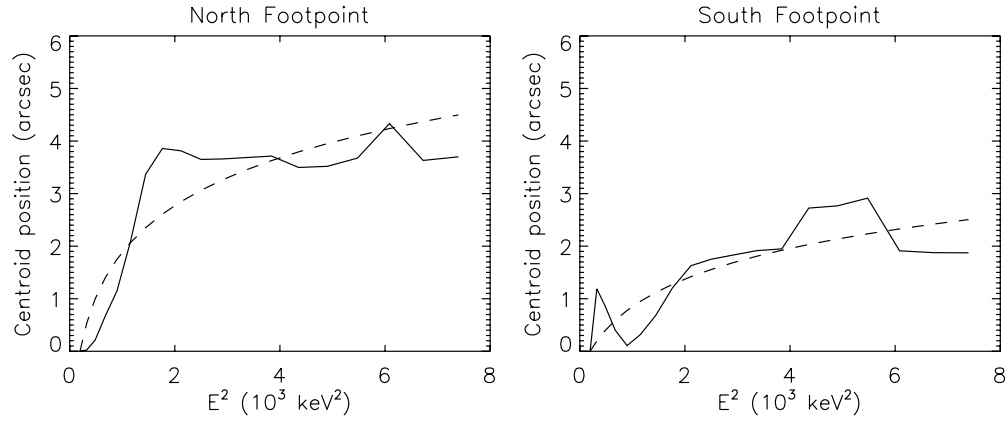


Figure 3. Projected position of the electron centroid locations s_c^E , for both “north” and “south” footpoints, along the respective mean trend lines (solid curves; cf. Figure 2). Superimposed (dashed curve) on each plot is the fit to the analytic exponential atmosphere model. The parameters of the fits are provided in the text.

2. The values of N_0 differ by over 2 orders of magnitude; they correspond to the stopping depths for electrons of energies ~ 1.5 keV and ~ 25 keV, respectively. Comparison with the overlying coronal mass column densities $m_0 \simeq 1.7 \times 10^{-24} N_0$ in various empirical solar models (Figure 1 and Tables 3 and 4 of Machado et al. 1980) show that the best-fit overlying column density $N_0 \simeq 6.3 \times 10^{19} \text{ cm}^{-2}$ for the “south” footpoint lies midway between the values for a plage and a weak “F1” flare, consistent with the strength of the 2002 February 20 event. The value $N_0 \simeq 2.5 \times 10^{17} \text{ cm}^{-2}$ for the “north” footpoint is anomalously low—it is over an order of magnitude less than for the quiet-Sun “QS” model of Machado et al. (1980). While this could in principle be accounted for by an acceleration region very close ($\ell \sim N_0/n_0 \simeq 10^6$ cm) to the “north” footpoint, such an asymmetry in the acceleration region relative to the two footpoints should also be manifested in a spectral index difference between the two footpoints, a difference that is not observed. It is also worth noting that acceptable fits to the data occur for significantly larger values of N_0 up to a few $\times 10^{18} \text{ cm}^{-2}$, so that there may not be any issue of substance here.
3. The values of $H \sim (4 \pm 1) \times 10^8$ cm are comparable and, at first sight, unexpected—they are over an order of magnitude larger than the quiet-Sun atmospheric scale height $H = kT/m_p g \simeq 2 \times 10^7$ cm for an ambient chromospheric temperature $T \sim 6000$ K. (Here $k = 1.38 \times 10^{-16}$ erg K^{-1} is Boltzmann’s constant, $m_p = 1.67 \times 10^{-24}$ g is the proton mass, and $g = 2.74 \times 10^4 \text{ cm s}^{-2}$ the solar gravity.) For this factor of 20 discrepancy in H to be accounted for through non-vertical beam propagation would require propagation at a direction cosine to the vertical $\mu \sim (2 \times 10^7 / 4 \times 10^8) = 0.05$. Unless caused by magnetic scattering in a region of very high magnetic field gradient near the footpoint, this very small value of μ would require the initial acceleration to be in a near horizontal direction, in turn reducing the overlying vertical column densities N_0 by a factor of 20, to $1.2 \times 10^{16} \text{ cm}^{-2}$ and $3 \times 10^{18} \text{ cm}^{-2}$, respectively. Both these values of N_0 are so unlikely that we can reject non-vertical propagation of the beam as an explanation for the large values of H obtained. For vertical propagation of the electron beam, the inferred values of H would imply, for a static atmosphere, a temperature $T \sim 150,000$ K. However, the flaring atmosphere is patently *not* static, and the inferred values

of H may simply be indicative of the expanding density profile of the solar atmosphere in response to hydrodynamic forcing. Since the duration of the observations used was $\Delta t = 40$ s, we compared these results with the $t = 30$ s and $t = 40$ s density profiles in Figure 2 of the hydrodynamic simulations of Mariska et al. (1989). That figure shows that the density profile is considerably flattened as a result of the hydrodynamic response to heating by the flare-accelerated electrons: the slope $d \log n / ds$ in the upper chromospheric region $\simeq 1.5 \times 10^{-9} \text{ cm}^{-1}$, corresponding to a scale height $H = (1 / \ln 10) ds / d \log n \simeq 3 \times 10^8$ cm, in remarkably good agreement with the values deduced from the fitting procedure above.

Finally, it should also be noted, as remarked above, that the “south” footpoint has a complex structure, which would affect the interpretation of the best-fit values above.

4. SUMMARY

In this paper, we have validated the concept of using centroids as a parameter to describe the “location” of a compact source. It is worth stressing that the determination of the location of peak flux in an image requires evaluation of a spatial derivative of the image brightness and so data from the finest-resolution detectors available. By contrast, the centroid represents an *integral moment* of the source image and so can be measured using detectors with relatively coarse angular resolution. In the case of *RHESSI*’s RMC design, sources with dimension much less than the angular resolution of the coarsest-resolution RMC gradually emerge from being occulted by the RMC slats as the spacecraft rotates; the “rising” of the source centroid is marked by the observed flux reaching 50% of its peak value, and accurate timing of this instant permits the determination of the centroid to the high precision.

Theoretical forms derived for the energy-dependent position of the centroid of the electron flux distribution position (e.g., Equations (7) and (14)) permit ready comparison of models with data. Examination of the variation of the centroid position in electron maps of the 2002 February 20 flare allowed us to derive values of the parameters of the density structure of the target atmosphere; these values were found to be consistent with a non-static atmosphere driven by flare heating.

Ma.P., A.M.M., and Mi.P. were supported by contract I/015/07/0 between the Italian ASI and the Italian INAF, and

A.G.E. by NASA grant NNG04G063G and by subcontract SA4878-26308 from the University of California, Berkeley. E.P.K. acknowledges the financial support of an STFC rolling grant, an STFC/PPARC Advanced Fellowship, and the Leverhulme Trust. Financial support by the European Commission through the SOLAIRE Network (MTRN-CT-2006-035484) is gratefully acknowledged. The overall effort has greatly benefited from support by a grant from the International Space Science Institute (ISSI) in Bern, Switzerland.

APPENDIX

LOCATION OF PEAK ELECTRON FLUX FOR AN EXPONENTIALLY STRATIFIED TARGET

As an alternative to the source centroid, Aschwanden et al. (2002) and Brown et al. (2002) used the location of the *maximum value* in the intensity profile of the photon emission. For completeness, we here present the equivalent analysis for the location of the maximum in the function $n(s)F(E, s)$, the density-weighted electron flux as a function of distance s along the propagation direction.

For a power-law injected spectrum, we have, from Equation (4)

$$n(s)F(E, s) = (F_b E E_b^\delta) n(s) \times \left(E^2 + 2K \int_{-\infty}^s n(s') ds' \right)^{-(\delta+1)/2}. \quad (\text{A1})$$

The position of the maximum of $n(s)F(E, s)$ can be found by differentiating Equation (A1) with respect to s , resulting in the following implicit equation for s_{\max} :

$$\left(E^2 + 2K \int_{-\infty}^{s_{\max}} n(s') ds' \right) \left(\frac{dn}{ds} \right)_{s=s_{\max}} = (\delta + 1)K[n(s_{\max})]^2. \quad (\text{A2})$$

A reasonable representation of $n(s)$ for vertical propagation in the solar chromosphere is (Kontar et al. 2008) the exponential

density profile $n(s) = n_0 e^{s/H}$, where H is a scale height. With this, Equation (A2) leads to

$$(\delta - 1) e^{s_{\max}/H} = \frac{E^2}{Kn_0H} - 2, \quad (\text{A3})$$

leading to the following explicit expression for s_{\max} :

$$s_{\max}(E; \delta, n_0, H) = H \ln \left[\frac{\frac{E^2}{Kn_0H} - 2}{\delta - 1} \right]. \quad (\text{A4})$$

(Note that for $E^2 < (\delta + 1)Kn_0H$, the function $n(s)F(E, s)$ is monotonically decreasing in $s > 0$ and no local maximum exists.)

REFERENCES

- Aschwanden, M. J., Brown, J. C., & Kontar, E. P. 2002, *Sol. Phys.*, **210**, 383
- Brown, J. C. 1971, *Sol. Phys.*, **18**, 489
- Brown, J. C. 1972, *Sol. Phys.*, **26**, 441
- Brown, J. C., Aschwanden, M. J., & Kontar, E. P. 2002, *Sol. Phys.*, **210**, 373
- Emslie, A. G. 1978, *ApJ*, **224**, 241
- Emslie, A. G., Miller, J. A., & Brown, J. C. 2004, *ApJ*, **602**, 69
- Emslie, A. G., & Smith, D. F. 1984, *ApJ*, **279**, 882
- Hurford, G. J., Schwartz, R. A., Krucker, S., Lin, R. P., Smith, D. M., & Vilmer, N. 2003, *ApJ*, **595**, 77
- Hurford, G. J., et al. 2002, *Sol. Phys.*, **210**, 61
- Kontar, E. P., & Brown, J. C. 2006, *ApJ*, **653**, L109
- Kontar, E. P., Hannah, I. G., & MacKinnon, A. L. 2008, *A&A*, **489**, L57
- Lin, R. P., et al. 2002, *Sol. Phys.*, **210**, 3
- Machado, M. E., Avrett, E. H., Vernazza, J. E., & Noyes, R. W. 1980, *ApJ*, **242**, 336
- Mariska, J. T., Emslie, A. G., & Li, P. 1989, *ApJ*, **341**, 1067
- Massone, A. M., Emslie, A. G., Hurford, G. J., Prato, M., Kontar, E. P., & Piana, M. 2009, *ApJ*, **703**, 2004
- Massone, A. M., Emslie, A. G., Kontar, E. P., Piana, M., Prato, M., & Brown, J. C. 2004, *ApJ*, **613**, 1233
- Piana, M., Massone, A. M., Hurford, G. J., Prato, M., Emslie, A. G., Kontar, E. P., & Schwartz, R. A. 2007, *ApJ*, **665**, 846
- Xu, Y., Emslie, A. G., & Hurford, G. J. 2008, *ApJ*, **673**, 576